

## Comparative study on dynamic properties of argillaceous siltstone and its grouting-reinforced body

Ming Huang<sup>\*1,2</sup>, Chao-Shui Xu<sup>2</sup>, Jin-Wu Zhan<sup>1</sup> and Jun-Bao Wang<sup>3</sup>

<sup>1</sup> College of Civil Engineering, Fuzhou University, Fuzhou 350108, China

<sup>2</sup> School of Civil, Environment and Mining Engineering, the University of Adelaide, Adelaide 5005, Australia

<sup>3</sup> School of Civil Engineering, Xi'an University of Architecture and Technology, Xi'an 710055, China

(Received June 01, 2016, Revised February 03, 2017, Accepted March 15, 2017)

**Abstract.** A comparison study is made between the dynamic properties of an argillaceous siltstone and its grouting-reinforced body. The purpose is to investigate how grout injection can help repair broken soft rocks. A slightly weathered argillaceous siltstone is selected, and part of the siltstone is mechanically crushed and cemented with Portland cement to simulate the grouting-reinforced body. Core specimens with the size of 50 mm × 38 mm are prepared from the original rock and the grouting-reinforced body. Impact tests on these samples are then carried out using a Split Hopkinson Pressure Bar (SHPB) apparatus. Failure patterns are analyzed and geotechnical parameters of the specimens are estimated. Based on the experimental results, for the grouting-reinforced body, its shock resistance is poorer than that of the original rock, and most cracks happen in the cementation boundaries between the cement mortar and the original rock particles. It was observed that the grouting-reinforced body ends up with more fragmented residues, most of them have larger fractal dimensions, and its dynamic strength is generally lower. The mass ratio of broken rocks to cement has a significant effect on its dynamic properties and there is an optimal ratio that the maximum dynamic peak strength can be achieved. The dynamic strain-softening behavior of the grouting-reinforced body is more significant compared with that of the original rock. Both the time dependent damage model and the modified overstress damage model are equally applicable to the original rock, but the former performs much better compared with the latter for the grouting-reinforced body. In addition, it was also shown that water content and impact velocity both have significant effect on dynamic properties of the original rock and its grouting-reinforced body. Higher water content leads to more small broken rock pieces, larger fractal dimensions, lower dynamic peak strength and smaller elastic modulus. However, the water content plays a minor role in fractal dimensions when the impact velocity is beyond a certain value. Higher impact loading rate leads to higher degree of fragmentation and larger fractal dimensions both in argillaceous siltstone and its grouting-reinforced body. These results provide a sound basis for the quantitative evaluation on how cement grouting can contribute to the repair of broken soft rocks.

**Keywords:** ground reinforcement; broken soft rock; Split Hopkinson Pressure Bar; cement grouting; grouting-reinforced body; dynamic mechanical-property; cement grouting

### 1. Introduction

Cement grouting is commonly used for ground reinforcement in tunnels and slopes. It is typically applied to operations where in-situ rocks or soils have poor mechanical properties which

---

\*Corresponding author, Associate Professor, E-mail: [huangming05@163.com](mailto:huangming05@163.com)

cannot satisfy the stability requirements. There are significant published works in the literature on the assessment of the effects of cement grouting on the improvement of rock mass mechanical properties. Kikuchi *et al.* (1997) employed in-situ rock mechanical tests and geophysical methods (such as electromagnetic wave, elastic wave prediction and borehole expansion test) to investigate the grouting effects on rock quality. It was found that the characteristics of the rock mass become more uniform due to grouting which are confirmed by the observations of increasing elastic wave velocity and rock mass deformation modulus. Yang and Li (2008) conducted two geophysical sonic wave surveys before and after grouting and they detected an increment of about 5.7% in the wave velocity, changing from 5300 m/s to 5600 m/s on average. Di and Wang (2010) performed a 2D resistivity survey using multi-electrode resistivity system along the Da Ye Dam foundation and they found that the rock appeared more homogeneous with no obvious anomalies recorded after the dam foundation was grouted. Li and Wu (2013) analyzed the effect of grouting reinforcement on the stress and deformation of rock masses using numerical simulation models and they concluded that the stress and displacement of rock masses become more symmetrical and continuous after grouting. Utsuki (2013) conducted in-site tests on five types of rocks in 14 places at nine dam sites before and after grouting and quantitatively examined the deformability of rock masses in detail from these experimental results. They found that the deformation modulus after grouting was larger than that before grouting at almost all the measurement points. The increment of the modulus varied depending on the original geological conditions, with a smaller increment generally for a higher original modulus.

Zolfaghari *et al.* (2015) developed a Q-logging system based on core samples drilled at grouting panels to investigate the influence of cement grouting on the rock mass properties at the Bakhtiary dam site. Rock masses in different boreholes at grouting panels were classified using the proposed Q-logging system and it was shown that the Q-logging system can be used as a practical and undemanding method for quality evaluation of grouted rock masses. Xu *et al.* (2013) developed the strength growth theory for broken rocks before and after grouting based on the Mohr-Coulomb strength criterion, where the equations of the growth rates for uniaxial compressive strength, tensile strength, cohesion and internal friction coefficient were given. Most previous studies, however, focus on static characteristics of broken rocks and their grouting-reinforced bodies, e.g., experimental tests and theoretical estimations on the static strength of the grouting-reinforced body. Research on dynamic characteristics of grouting-reinforced body is rarely reported. With the advance in large-diameter split Hopkinson pressure bar (SHPB) apparatus and its capability to handle large-dimension specimens of heterogeneous materials such as rock and concrete in laboratory (Jiang and Vecchio 2009, Zhang *et al.* 2009), the technique has become an ideal choice to study the dynamic constitutive relation and dynamic mechanical parameters of rocks under high strain rate. Many researchers have reported successful applications of the technique on the investigation of dynamic behavior of materials (Li and Tao 2015, Lu *et al.* 2010, Wang *et al.* 2010, Hsiao *et al.* 2016, Chen *et al.* 2016, Dai *et al.* 2010, Zhou *et al.* 2011).

Dynamic mechanical-properties of broken soft rock after grouting are of great importance as they directly affect the stability of the excavation under in-situ dynamic loading conditions. Therefore, relevant studies on the improvement in rock mass dynamic strength after grouting are of great practical significance. In this research, typical soft rock samples were collected from the project site, mechanically crushed and then used to prepare grouting-reinforced rock specimens. Unlike previous tests, the SHPB loading device with a large diameter of  $\varnothing 74$  mm was used in this work to study, both qualitatively and quantitatively, the dynamic properties of the original argillaceous siltstone and its grouting-reinforced body under different water-bearing states so as to

evaluate the improvement in mechanical properties of broken soft rocks after grouting. The fractal features of fragmented specimens of both the original rock and its grouting-reinforced body after impact failure were also compared. In addition, the characteristic stress-strain curves for both groups of tests at different water contents and different proportions of grouting cement were analyzed. Based on the observed differences between their mechanical damages, two damage mechanics models suitable to describe the dynamic failure characteristics of the original rock and its grouting-reinforced body are proposed.

## 2. Experiments and comparison study of fragmented samples

### 2.1 Specimen preparations

Typical argillaceous siltstone is sampled from the project site which is then cut into rock cylinder specimens with an approximate dimension of  $\text{Ø}50 \text{ mm} \times \text{H}38 \text{ mm}$  according to the requirements set by the SHPB apparatus, as shown in Figs. 1 and 2. In terms of water content of the rock, as shown in Table 1, samples 7-1 and 7-2 are rocks in saturated state, 8-1 and 8-2 correspond to the state of natural water absorption (absorption state) at room temperature, and 9-1 and 9-2 are natural water-bearing state (natural state, not immersed in water). Samples 7-1, 8-1 and 9-1 are tested using the impact velocity of 14.51 m/s, while 7-2, 8-2 and 9-2 are tested using the impact velocity of 18.80 m/s.

To prepare the grouting-reinforced rock specimens, the original rock sample was mechanically crushed into rock pieces with the particle diameter ranging from 5.0 to 10.0 mm. A mold was used to prepare a cube model (through dry and wet mixing). 42.5 ordinary Portland cement (OPC),



Fig. 1 Specimen preparation

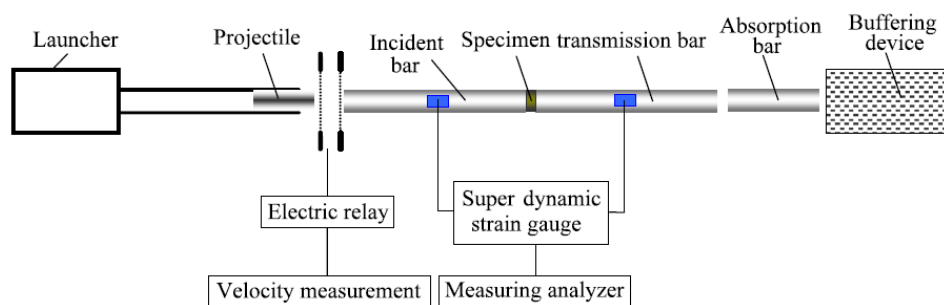


Fig. 2 Experimental setup (Li and Xu 2009, Bailly *et al.* 2011)

Table 1 Specimens of argillaceous siltstone

No.	Dimensions			Water content (%)
	Diameter (mm)	Height (mm)	Cross section area (mm <sup>2</sup> )	
7-1	49.42	36.73	1815.197	0.96
7-2	49.58	38.54	1910.813	0.88
8-1	49.55	38.01	1883.396	0.65
8-2	49.61	37.16	1843.508	0.62
9-1	49.64	38.24	1898.234	0.57
9-2	49.56	38.03	1884.767	0.54

Table 2 Specimens of grouting-reinforced body

No.	Dimensions			Portland cement (g)	Broken soft rock (g)	Water (g)	Average water content (%)	
	Diameter (mm)	Height (mm)	Cross section area (mm <sup>2</sup> )					
Natural state	4-1N	49.85	37.71	1951.73	320	1731	290	2.82
	4-2N	49.43	39.03	1918.98	380	1650	290	3.51
	4-3N	49.37	38.43	1914.33	440	1578	290	3.67
	4-4N	49.13	37.09	1895.76	500	1464	290	5.70
	4-5N	49.54	39.14	1927.53	560	1324	290	3.56
Absorption state	4-1A	49.57	38.47	1929.87	320	1731	290	7.86
	4-2A	48.76	37.96	1867.31	380	1650	290	6.35
	4-3A	49.48	37.19	1922.87	440	1578	290	8.87
	4-4A	49.42	38.88	1918.21	500	1464	290	5.95
	4-5A	48.69	37.80	1861.96	560	1324	290	8.76
Saturated state	4-1S	49.45	37.78	1920.54	320	1731	290	14.29
	4-2S	48.96	38.57	1882.66	380	1650	290	9.51
	4-3S	49.25	38.03	1905.03	440	1578	290	12.66
	4-4S	49.13	38.95	1895.76	500	1464	290	10.22
	4-5S	49.49	37.09	1923.64	560	1324	290	11.77

typically used for tunnel construction, was then used to grout the crushed rocks within the mold. The cement grout was applied continuously until the void between broken rocks was completely filled to simulate the application of grouting in broken rock masses in practice. After curing, the grouting-reinforced body was cut into rock cylindrical specimens of about the dimension of  $\varnothing 50$  mm  $\times$  H38 mm as shown in Table 2. Samples 4-1S to 4-5S are rocks in saturated state, 4-1A to 4-5A correspond to the state of natural water absorption (absorption state) at room temperature, and 4-1N to 4-5N are natural water-bearing state (natural state, not immersed in water).

By comparing the water contents in Tables 1 and 2, it is obvious that the original rock has generally lower water contents in different states, which suggests that the argillaceous siltstone has a relatively denser internal structure with smaller pore volume and lower connectivity between internal pores. Compared to the original rock, however, the grouting-reinforced body,

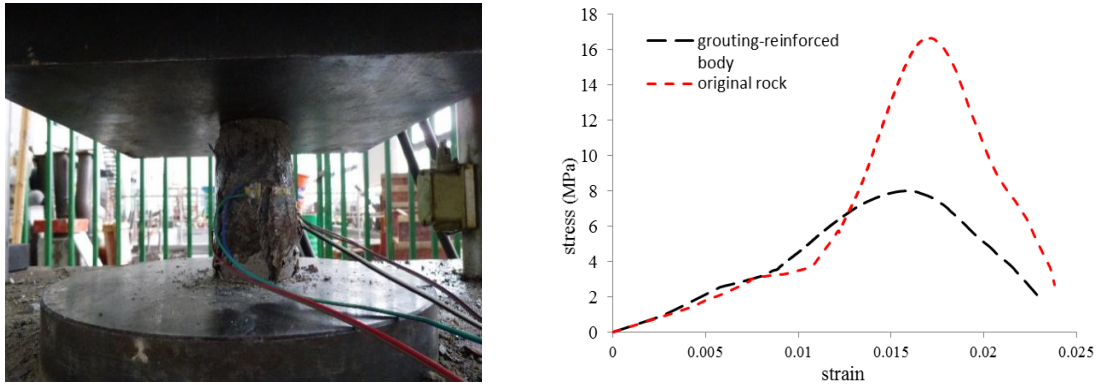


Fig. 3 Uniaxial compression test of the samples

Table 3 Mechanical properties the original rock and its grouting-reinforced body

Samples	Uniaxial compression strength (MPa)	Corresponding strain	Elastic modulus (GPa)
Original rock	16.67	0.017	1.823
Grouting-reinforced body	8.04	0.016	0.834

which can be regarded as an artificial rock, is formed by cementing together loosely packed broken rock particles and therefore the volume of internal pores is expected to be higher. During the cement solidification process, fine cracks may grow on the boundary between rock particle and the grouting slurry which will act as effective connection pathways between pore structures within the body. Once in a water-rich environment, these cracks can easily absorb and transport water and the body can reach the absorption state at normal temperature and pressure relatively quickly. Consequently the water content of the grouting-reinforced body is always higher than that of the original rock after the specimen is fully saturated.

In addition, to compare the quasi-static mechanical properties of the original rock and its grouting-reinforced body, two cylindrical samples with the dimension of  $\varnothing 50 \text{ mm} \times H100 \text{ mm}$  under natural water-bearing state were prepared. Uniaxial compression tests were then carried out using a servo-control machine, as shown in Fig. 3, and the test results are given in Table 3. For the grouting-reinforced rock specimen, the uniaxial compression strength is 8.04 MPa, compared with 16.67 MPa of the original rock. Observations of the failure of grouting-reinforced rock specimens indicated that most cracks occur in cementation boundaries between the cement mortar and the original rock particles, which suggests that cementation boundaries have lower quasi-static strength compared with the original rocks. Uniaxial compression strength of grouting-reinforced body is lower than that of original rock. However, it is obvious that strength recovery for the fractured rock mass can be achieved using the grouting technology.

## 2.2 Comparison study of sample fragmentation

In order to compare the fragmentation patterns, both the original and the grouting-reinforced rock specimens are impacted at the same speed of 18.80 m/s. Fig. 4 shows the failure patterns of the original rock specimens and the grouting-reinforced rock specimens of group 4-4. From



Fig. 4 Failure characters of specimens under different water-bearing states at the same impact velocity

observation, when the specimens are impacted, initial cracks initiate densely along the impact direction and continue to grow along the axial directions until eventually coalesce to form broken pieces. For the grouting-reinforced rock specimens, apart from the characteristics mentioned above, it is also clear that most of the cracks occur in cementation boundaries between the cement mortar and the original rock particles, suggesting that these boundaries have the lowest dynamic strength compared with the original rock pieces and the cement mortar, which is expected. This also explains the reason that the grouting-reinforced body has lower strength and is generally more fragmented after impact. For size distributions, the fragments are passed through a serial of sieves to obtain the data shown in Tables 4 and 5. The data show that for the original rock fragments, particles with a diameter over 20 mm account for more than 50% of the total mass. For the grouting-reinforced rock fragments, the corresponding proportion is zero for most cases, where

Table 4 Mass percentage (%) of particle groups of fragments for the original rock

No.	> 20 (mm)	10~20 (mm)	5~10 (mm)	2~5 (mm)	0.5~2 (mm)	0.25~0.5 (mm)	< 0.25 (mm)
7-1	58.849	22.676	11.155	4.750	2.098	0.351	0.122
8-1	63.099	23.201	9.873	2.575	1.142	0.104	0.005
9-1	66.931	18.224	10.156	2.998	1.486	0.190	0.015
7-2	44.027	34.498	14.574	3.500	2.669	0.388	0.343
8-2	58.220	25.045	9.502	4.147	2.398	0.459	0.230
9-2	47.093	37.512	12.608	1.478	0.727	0.323	0.258

Table 5 Mass percentage (%) of particle groups of fragments for grouting-reinforced body

No.	> 20 (mm)	10~20 (mm)	5~10 (mm)	2~5 (mm)	0.5~2 (mm)	0.25~0.5 (mm)	< 0.25 (mm)
4-1 (Nat)	8.055	12.574	34.479	26.817	13.971	1.353	2.751
4-2 (Nat)	0.000	10.498	31.902	39.264	13.870	1.536	2.930
4-3 (Nat)	0.000	7.870	34.491	36.111	14.755	2.143	4.630
4-4 (Nat)	5.490	19.137	24.549	33.255	12.542	1.733	3.294
4-5 (Nat)	12.437	24.286	24.118	25.210	9.285	1.975	2.689
4-1 (Abs)	7.772	14.508	38.549	27.047	8.573	1.893	1.658
4-2 (Abs)	0.000	13.688	30.757	36.715	14.177	1.523	3.140
4-3 (Abs)	0.000	8.978	31.579	37.229	15.080	3.341	3.793
4-4 (Abs)	0.000	9.974	30.876	38.161	15.891	2.236	2.862
4-5 (Abs)	3.889	9.722	26.296	38.426	14.631	3.425	3.611
4-1 (Sat)	0.000	8.043	32.096	37.200	15.868	2.461	4.332
4-2 (Sat)	0.000	7.670	37.389	37.242	11.575	3.543	2.581
4-3 (Sat)	0.000	2.691	32.556	37.489	18.602	2.564	6.098
4-4 (Sat)	0.000	8.835	31.708	39.431	12.641	3.513	3.872
4-5 (Sat)	0.000	11.450	33.935	35.808	11.416	4.753	2.638

particles with the largest mass proportion mostly have a diameter range of 2~5 mm. In addition, water content also affects the rock breakage. The higher the water content, the higher the degree of fragmentation. This suggests that the present of water actually accelerates the development of cracks within the samples, and induces reduction in strength of the soft rock, which is consistent with the experiments reported by Erguler and Ulusay (2009).

### 2.3 Fractal characteristics of the fragments

Many results from damage evolution experiments on brittle fracture of rocks suggest some statistical self-similarity, or fractal characteristics in the fracture patterns. These self-similarity features can be found not only at the macro, but also at the micro scales (Nolen-Hoeksema and Gordon 1987). The definition of continuum fractal can be given as (Xie 1993)

$$N = CR^{-D} \quad (1)$$

where,  $R$  is the characteristic scale,  $N$  is objection quantity at the characteristic scale  $R$ ,  $C$  is the proportional constant, and  $D$  is the fractal dimension. The increment in  $N$  due to the increment in  $R$  is then

$$dN \propto R^{-D-1}dR \quad (2)$$

On the other hand, the change in quantity  $N$  due to the change in the mass  $M$  corresponding to a certain scale  $R$  have the following approximate geometrical relationship (Xie 1993)

$$dN \propto R^{-3}dM \quad (3)$$

In our experiments, a large number of fragments are produced and it is difficult and impractical

to measure the exact number ( $N$ ) of fragments using the scale-frequency method. Therefore, the size-frequency distribution of fragments is adopted (Ghanbarian and Daigle 2015)

$$M(R)/M_T = 1 - \exp[-(R/\sigma)^a] \quad (4)$$

where  $M(R)$  is the mass of fragments smaller than  $R$  in diameter,  $M_T$  is total mass,  $\sigma$  is a variable related to the average size, and  $a$  is defined below.

If  $R/\sigma \ll 1$ , the equation above can be approximated using a power law relationship

$$M(R)/M_T = (R/\sigma)^a \quad (5)$$

and therefore

$$dM \propto R^{a-1} dR \quad (6)$$

By combining Eqs. (2), (3) and (6), the following relationship can be obtained

$$R^{-D-1} \propto R^{-3} R^{a-1} = R^{a-4} \quad (7)$$

and therefore

$$D = 3 - a \quad (8)$$

where  $a = \ln(M_{L_{eq}}/M)/\ln L_{eq}$ ,  $M_{L_{eq}}/M$  is the cumulative mass proportion of the fragments with an equivalent side length smaller than  $L_{eq}$ ,  $M_{L_{eq}}$  is the mass of fragments with an equivalent side length smaller than  $L_{eq}$ , and  $M$  is the total mass of fragments within the calculation scale (Liu *et al.* 2012).  $D$  of Eq. (8) is the mass fractal dimension, or the fractal dimension of particle-size distribution. This dimension parameter was calculated for our tests and the results are shown in Table 6. The correlation coefficients given in the table indicate reliability of the calculated values. The grouting-reinforced body generally has larger fractal dimensions ( $> 2.1$ ), compared with the original rock at the same impact velocity, as it contains more small broken pieces, as demonstrated in Fig. 4.

Table 6 Fractal dimension of the fragmentation of specimens after impact

WBS Name	No.	FD	CC	WBS Name	No.	FD	CC	WBS Name	No.	FD	CC
OR	9-1	1.356	0.965	OR	8-1	1.113	0.962	OR	7-1	1.706	0.994
	9-2	1.864	0.933		8-2	1.859	0.996		7-2	1.867	0.992
	4-1N	2.129	0.983		4-1A	2.035	0.987		4-1S	2.220	0.978
NS	4-2N	2.113	0.976	AS	4-2A	2.134	0.979	SS	4-2S	2.127	0.977
GB	4-3N	2.231	0.979	GB	4-3A	2.205	0.979	GB	4-3S	2.294	0.974
	4-4N	2.174	0.984		4-4A	2.124	0.975		4-4S	2.210	0.978
	4-5N	2.170	0.993		4-5A	2.206	0.976		4-5S	2.156	0.973

WBS—water bearing state, FD—fractal dimension, CC—correlation coefficient,  
 OR—original rock, GB—grouting-reinforced body, NS—natural state,  
 AS—absorption state, SS—saturate state

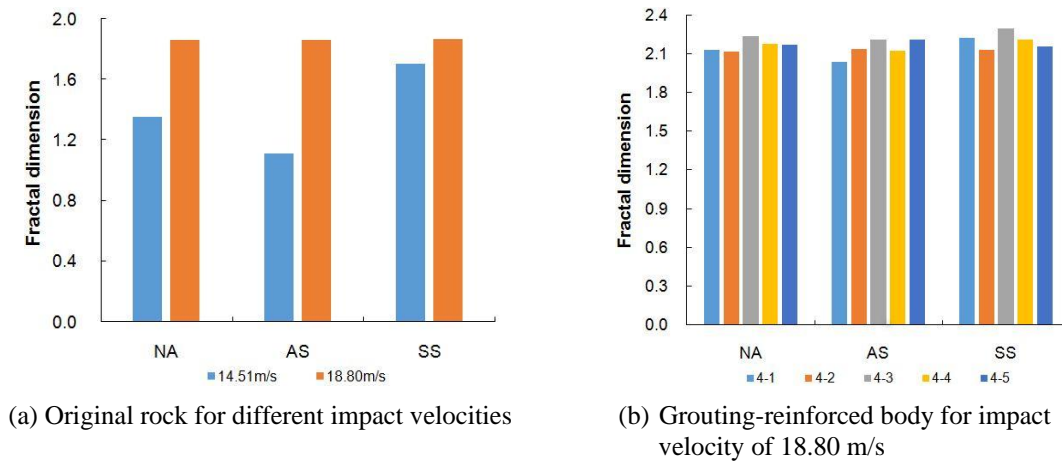


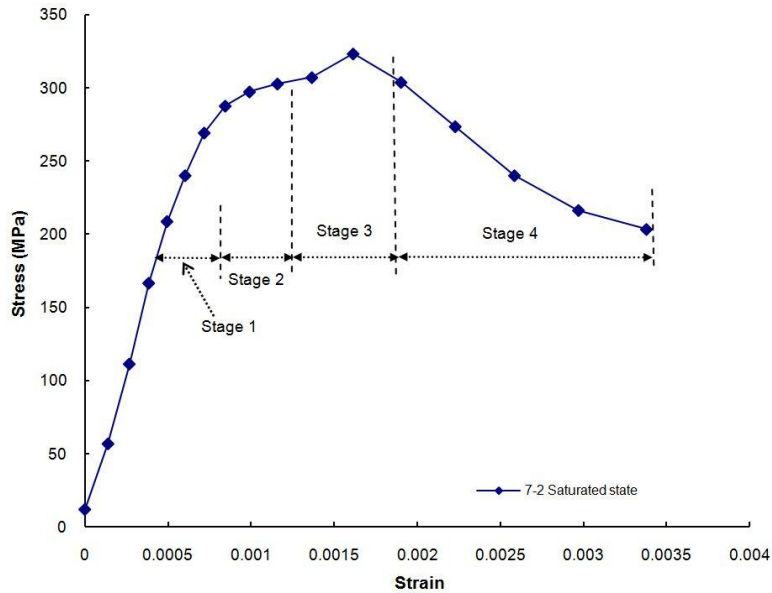
Fig. 5 Fractal dimension of argillaceous siltstone and its grouting-reinforced body (AS — absorption state, NS — natural state, SS — saturate state)

At the lower impact velocity of 14.51 m/s, the fractal dimension of the original rocks increases with the increment in its water content as shown in Fig. 5(a), which indicates that higher water content results in larger fractal dimensions. However, this trend is not obvious at the higher impact velocity of 18.80 m/s, which suggests that the impact energy at higher velocity might be too high for this rock, so its effect is dominant and therefore the effect of different water content becomes insignificant. The same argument applies to the grouting-reinforced body for impact velocity of 18.80 m/s as no significant effect of water content is shown in Fig. 5(b).

### 3. Comparison study of dynamic stress-strain curves

#### 3.1 Shape features

Fig. 6 shows the measured stress-strain curves of original rock with different water contents at two impact velocities. The curves are similar in shape, and generally consist of the following four stages (Fig. 6(a)). The first is the approximate elasticity stage ( $d^2\sigma/d\varepsilon^2 \approx 0$ ). During this stage, the stress-strain relationship is approximately linear and the stress wave is reflected multiple times within the specimen until the stress and strain are uniformly distributed. The second stage is the micro-crack development stage ( $d^2\sigma/d\varepsilon^2 < 0$ ). During this stage, stress grows slowly with strain, and the curve follows an upward convex pattern. Micro-cracks in the specimen gradually propagate, and new cracks are also generated. Plastic deformation gradually becomes the dominant mode of deformation. The third stage is the unstable crack propagation stage where the strain rate increment is much higher compared with stage 2. Stress on the specimen is getting close to the peak value. A large number of small cracks coalesce to form major cracks. At the end of this stage, the stress reaches its maximum. The fourth stage is the strain softening stage ( $d\sigma/d\varepsilon < 0$ ). After the stress reaches its peak value, many major cracks are formed and the bearing capacity of the specimen drops rapidly while the specimen deformation is accelerated until the specimen breaks into pieces. Violent ejection of broken rock pieces due to stored residual energy is generally observed.



(a) Stages of the stress-strain curves

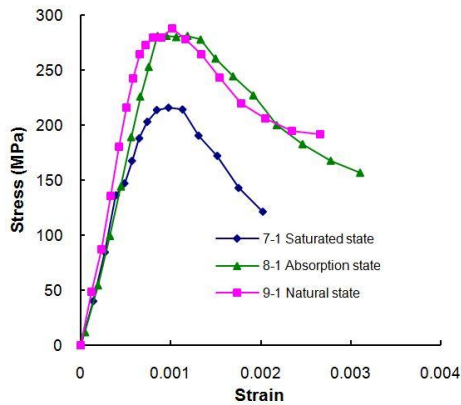
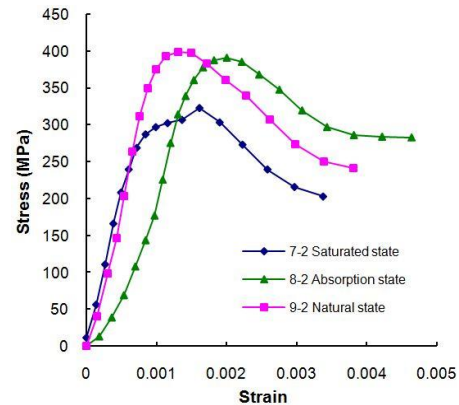
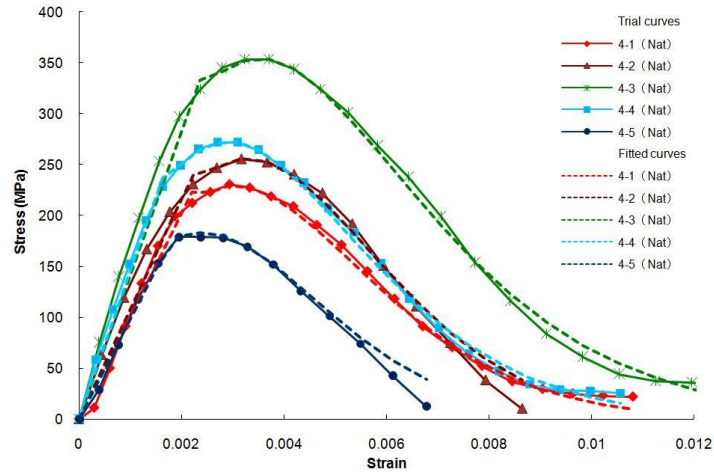
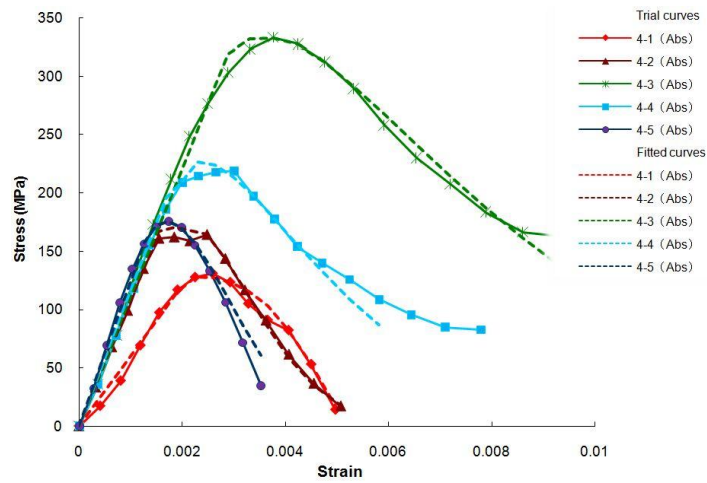
(b)  $v = 14.51$  (m/s)(c)  $v = 18.81$  (m/s)

Fig. 6 Dynamic stress-strain curves of argillaceous siltstone under different water-bearing states

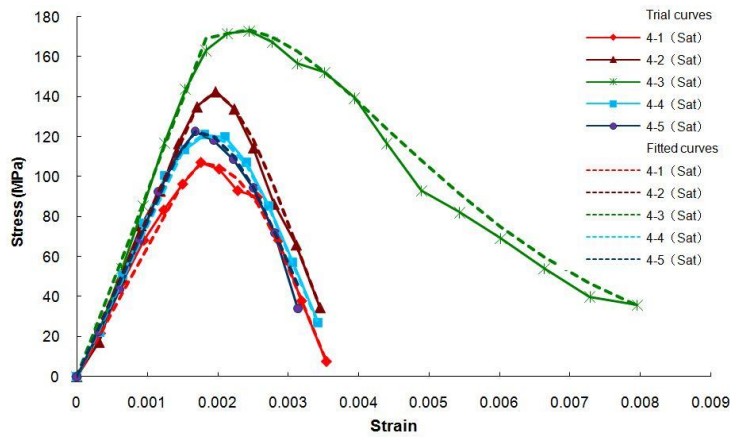
Fig. 7 shows the dynamic stress-strain curves of grouting-reinforced body at impact velocity of 18.80 m/s. They have stages similar to those of the original rock. Under impact, the grouting-reinforced body shows failure characteristics as obviously as the original rock, and it reaches its peak strength at a smaller strain compared with that under the static load. However, the dynamic peak strength of the original rock at the same impact velocity is generally higher but the post-peak strain softening behavior of grouting-reinforced body is more pronounced with a greater post-peak deformation before the specimen disintegrates into pieces. At the time of specimen failure, less residual energy is stored so the ejection of broken rock pieces is much less violent compared with original rock specimens. The maximum strain of the original rock at the time of complete failure is in the order of  $10^{-3}$ , while that for the grouting-reinforced body is  $10^{-2}$ , indicating that the grouting-reinforced body has a higher ductility than the original rock. Despite of its lower maximum



(a) Natural state



(b) Absorption state



(c) Saturated state

Fig. 7 Measured curves and theoretical curves of grouting-reinforced rock specimens

Table 7 Test parameters and results of original rock

No.	Water content (%)	Diameter (mm)	Height (mm)	Bullet velocity /(m/s)	Peak load /MPa	Strain corresponding to peak load ( $\mu\epsilon$ )	Elastic modulus /GPa
7-1	0.96	49.42	36.73		216.06	977	341.3
8-1	0.65	49.55	38.01	14.51	281.13	1188	405.2
9-1	0.57	49.64	38.24		287.74	1016	475.8
7-2	0.88	49.58	38.54		323.18	1213	472.4
8-2	0.62	49.61	37.16	18.80	391.03	2003	305.6
9-2	0.54	49.56	38.03		398.98	1307	495.7

bearing capacity, the good ductility of the grouting reinforced body may be a desirable character in many engineering applications for effective continuous control over deformation of rock mass under dynamic loading conditions.

### 3.2 Effect of water content

As shown in Table 7 and also Fig. 5, at the same impact velocity, there is little difference in the peak load for the original rock at natural and absorption water bearing state, though the rock at absorption state shows higher ductility at the impact velocity of 18.80 m/s. For the rock at saturated state where the water content is significantly higher, the peak load is much lower for both impact velocities even the stress-strain curves show similar profile, suggesting that the increase in water content will cause the dynamic strength of the rock to decrease. Under the same water-bearing state, the larger the loading rate, the higher the peak strength and the higher the strain corresponding to that peak strength, which is consistent to the general behavior of materials under dynamic loading conditions. Numbers in Table 7 also suggest loading rate has a much greater impact than water content on the mechanical behavior of the rock specimens.

Table 8 shows strength parameters of grouting-reinforced rock specimens with different water contents at the impact velocity of 18.80m/s. Compared with the original rock specimens, similar patterns are found. A higher water content leads to a lower dynamic peak strength and a smaller elastic modulus, suggesting the negative impact of water content on the bearing capacity of the rock. At the same impact velocity, elastic modulus and peak strength of the grouting-reinforced body are much smaller than those of the original rock. The difference between them in peak strength is close to 200 MPa under natural state, and 100 MPa under saturated state. The strain corresponding to the peak load for the grouting-reinforced body ranges from 1682  $\mu\epsilon$  to 3767  $\mu\epsilon$ , while that for the original rock ranges from 1213  $\mu\epsilon$  to 2003  $\mu\epsilon$ .

In addition, for the grouting reinforced body, a valuable result is found by examining the relationship between the peak strength and the mass ratio of rocks to cement slurry. The mass ratios of original rock to cement used in constructing our grouting reinforced body are 5.41:1, 4.34:1, 3.59:1, 2.93:1 and 2.36:1 respectively. The relationships between this ratio and the peak strength are shown in Fig. 8 for different water bearing states, where the optimal ratio to maximize the peak strength of the grouting reinforced body is clearly indicated to be around 3.59:1. The lower the mass ratio of rocks to cement, the larger the grouting volume, the flaw existing in the cement will determine the characteristics of the body. Conversely, high ratios correspond to more

Table 8 Experimental results grouting-reinforced body

No.	Bullet velocity /(m/s)	Peak load /MPa	Strain corresponding to peak load ( $\mu\epsilon$ )	Elastic modulus /GPa	
Natural state	4-1 (Nat)	230.49	2933	101.8	
	4-2 (Nat)	255.64	3166	108.4	
	4-3 (Nat)	18.80	353.48	3706	158.9
	4-4 (Nat)	271.91	3088	156.3	
	4-5 (Nat)	179.01	2363	98.6	
Absorption state	4-1 (Abs)	130.77	2588	64.0	
	4-2 (Abs)	164.19	2484	109.7	
	4-3 (Abs)	18.80	332.71	3767	116.5
	4-4 (Abs)	218.69	3004	120.8	
	4-5 (Abs)	175.58	1734	139.9	
Saturated state	4-1 (Sat)	106.99	1760	68.7	
	4-2 (Sat)	142.66	1970	78.6	
	4-3 (Sat)	18.80	172.84	2445	102.2
	4-4 (Sat)	121.04	1819	75.8	
	4-5 (Sat)	122.68	1682	72.1	

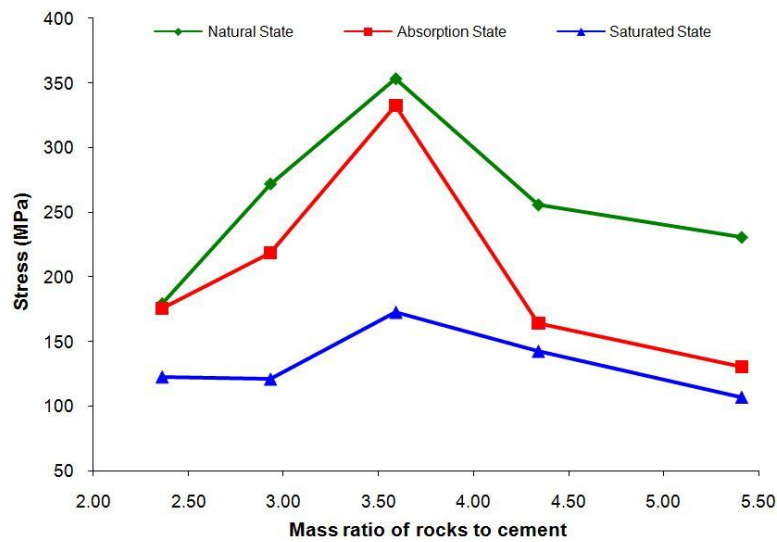


Fig. 8 Variation of peak strength with the mass ratio of rocks to cement

rock volume which eventually will result in lower strength because of the lack of bonding between rock particles. Based on these discussions, it can be assumed that the best grouting effect can be achieved when the mass ratio of rocks to cement is moderate and the condition for grout injection is good. This argument is consistent with the grout behavior demonstrated during the evaluation of actual grouting effect in rock engineering (Kikuchi *et al.* 1997, Xu *et al.* 2013).

#### 4. Theoretical models applied to this study

Dynamic constitutive relation of a rock mass reflects the combined macro-behavior of its intact rock component and internal macro- and meso-scale defects under dynamic load. For these defects, their damage and damage evolution due to external loading may significantly influence mechanical properties of the rock mass. Under impact load, the strain softening is dominant, outweighing strain hardening and strain rate strengthening behaviors (Wong and Chau 1998). Therefore, a reasonable dynamic damage constitutive model of rock must be able to reflect its damage softening and strain rate strengthening effects.

##### 4.1 Two common theoretical models

###### (1) Time dependent damage model

Based on thorough investigations into the constitutive characteristics of marble and granite, an impact-aging damage model involving a combination of a statistical damage model  $D_a$  and a viscoelastic body  $\eta$  was established (Shan *et al.* 2003), as shown in Fig. 9.

Strength of the statistical damage model  $D_a$  obeys the Weibull distribution, given as  $D_a = 1 - \exp\left[-\left(\frac{F}{F_0}\right)^m\right]$ , where  $F$  is the rock strength variable,  $m$  and  $F_0$  are the parameters of the Weibull distribution function. In addition, damage doesn't occur in the viscoelastic body  $\eta$ , given as  $\sigma = \eta \frac{d\varepsilon}{dt}$ . Therefore, the dynamic damage constitutive model of rock, suggested by Shan *et al.* (2003) is given according to the equivalent strain hypothesis

$$\sigma = E\varepsilon(1 - D_a) + \eta \cdot \frac{d\varepsilon}{dt} = E\varepsilon \exp\left[-\left(\frac{F}{F_0}\right)^m\right] + \eta \cdot \frac{d\varepsilon}{dt} \quad (9)$$

It is important to obtain proper values of relevant parameters to use equation (9), which can be derived from the stress-strain curve of the sample tested. If the peak strength and corresponding strain are  $\sigma_{\max}$  and  $\varepsilon_{\max}$ , the parameters are then given as  $F_0 = \left(a_0 + \frac{1}{\sqrt{3}}\right) E\varepsilon_{\max} \cdot m^{\frac{1}{m}}$ ,  $a_0 = \sin \varphi / \sqrt{9 + 3\sin^2 \varphi}$  and  $m = 1 / [\ln(E \cdot \varepsilon_m) - \ln(\sigma_{\max} - \eta \cdot d\varepsilon/dt)]$ . The parameters  $E$ ,  $\varepsilon_{\max}$ ,  $\sigma_{\max}$  and  $d\varepsilon/dt$  can be obtained directly from the testing curves. For parameters  $\eta$ ,  $\varphi$ , the values of  $\eta = 0.1$  and  $\varphi = 35$  (Liu and Tang 1999) are adapted in this paper.

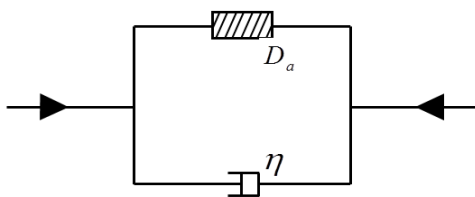


Fig. 9 Time dependent damage model

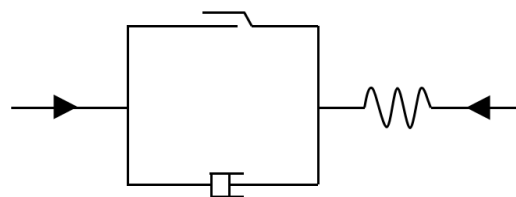


Fig. 10 Bingham model

## (2) Modified overstress damage model

Bingham model, usually known as an overstress model, can be employed to describe the dynamic behavior of rocks (Zhao *et al.* 2014), as illustrated in Fig. 10. In the original equation of the overstress model, the elastic modulus  $E_0$ , the compression yield strength  $S_0$  and the stress after failure  $S$  are not dynamic properties. Based on the Bingham model, a modified overstress model is derived to describe the dynamic mechanical behavior of viscoelastic materials. This modified model can better describe the transition from linear to non-linear behavior of the stress-strain curve (Dong and Shan 1999). However, the physical parameters involved in the model cannot be precisely defined. Zhao *et al.* (2014) introduced a loading rate dependent damage factors to overcome the deficiencies of this model, which was defined using  $1 - E_t/E$  in Shan *et al.* (2000). Considering the linear feature of the stress-strain curves at the initial loading stage, the modified damage constitutive equation is established as follows (Zhao *et al.* 2014)

$$\sigma = \begin{cases} E_0 \varepsilon & (\sigma < S_0) \\ \left\{ \sigma_s [1 + A(\varepsilon - \varepsilon_s)^B] \right\} \cdot \exp \left[ - \left( \frac{\varepsilon - \varepsilon_s}{\alpha} \right)^m \right] & S = \sigma_s \\ \left\{ \sigma_s [1 + A(\varepsilon - \varepsilon_{\max})^B] \right\} \cdot \exp \left[ - \left( \frac{\varepsilon - \varepsilon_{\max}}{\alpha} \right)^m \right] & S = \sigma_{\max} \end{cases} \quad (\sigma \geq S_0) \quad (10)$$

where  $m$ ,  $\alpha$  are shape factors of the Weibull distribution curve, and

$$A = (k\tau)^{\frac{1}{n}} \left( \frac{1}{\dot{\varepsilon}_0} \right)^{\frac{\zeta}{n}} (\dot{\varepsilon})^{\frac{\zeta}{n+1}}, B = \frac{b}{n} \quad (11)$$

where  $k$ ,  $\zeta$ ,  $b$ ,  $\tau$  and  $n$  are the statistic parameters of the rock material.

#### 4.2 Application of the models in our study

Fig. 11 shows the comparison between measured stress-strain curves and their best-fit curves based on the time dependent damage model (TDD model) and the modified overstress damage model (MOD model). For the original rock, best-fit curves from both models are close to measured ones, demonstrating a good approximation with correlation coefficients all above 0.9. This suggests that both models can be applied to describe the impact dynamic characteristics of argillaceous siltstone. For the grouting-reinforced body, however, the MOD performs much better than the TDD, suggesting that the time dependent damage model might not be a suitable model to describe the dynamic mechanical behavior of grouting-reinforced body.

Therefore to properly describe the dynamic mechanical behavior of the grouting-reinforced body for our case, the modified overstress damage model is adapted. Fitted parameters of the model based on the test data are listed in Tables 9 to 11 for different water bearing states. As shown in Fig. 7, the calculated values for the grouting-reinforced body follow closely the measured ones using the MOD. This suggests that this model could better describe the impact dynamic characteristics of the grouting-reinforced body and the model parameters obtained by curve fitting show in the tables are appropriate.

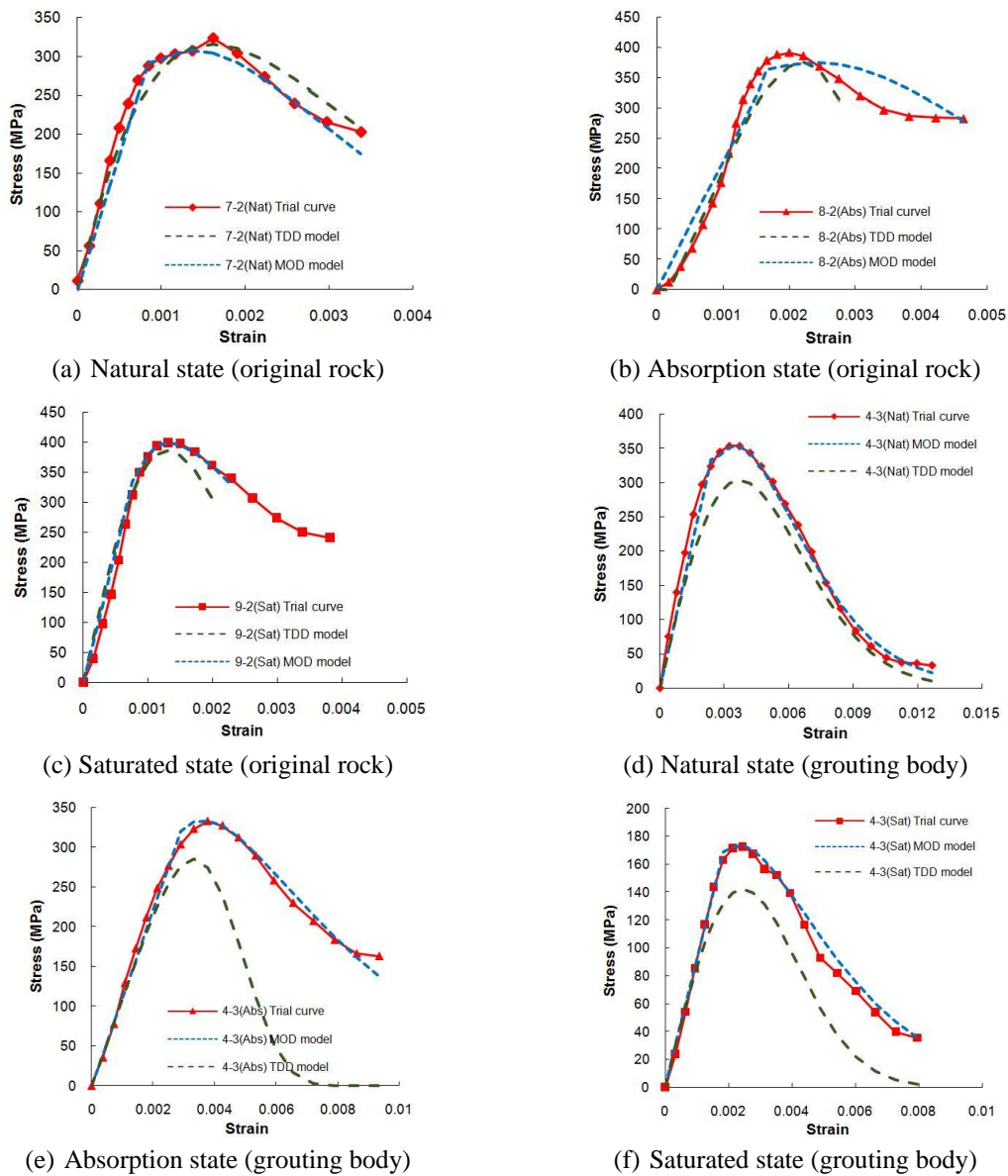


Fig. 11 Dynamic stress-strain fitting curves of argillaceous siltstone and its grouting-reinforced body

The best fit parameters are obviously related to other properties of the grouting-reinforced body. There is also a positive correlation between parameter  $A$  and  $B$  as the greater the absolute value of  $A$ , the greater the value of  $B$ . Some general relationships can be established from Tables 9~11. For example, the value of  $m$  fluctuate around 1.5 and the value of  $\alpha$  increases as the water content increases. The correlation between parameter  $B$  and elastic module  $E_0$  can be accurately described by a power function  $y = px^{-q}$ , as well as the correlation between parameter  $m$  and dynamic peak strength. The greater the  $E_0$ , the lower the value of  $B$ , and the greater the peak strength, the lower the value of  $m$ , as shown in Figs. 12 and 13, where the relationships for different water-bearing

Table 9 Fitting parameters of grouting-reinforced rock specimens under natural state

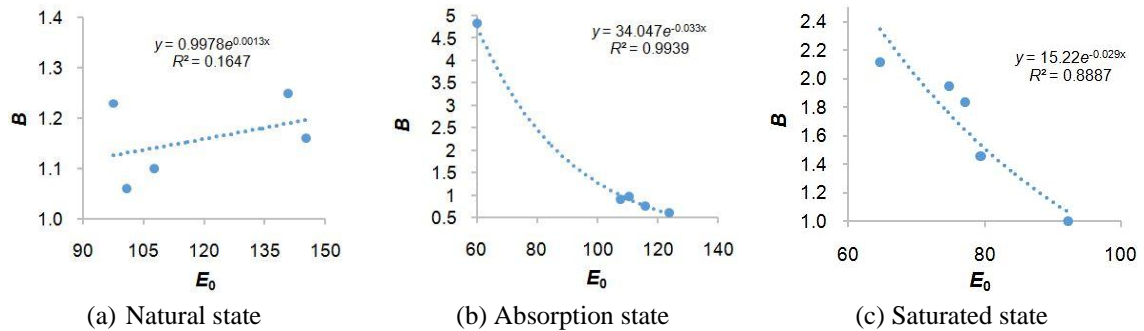
No.	Peak strength /MPa	$E_0$ /GPa	A	B	m	$\alpha (\times 10^{-2})$
4-1 (Nat)	230.49	100.8	321.62	1.06	1.46	0.305
4-2 (Nat)	255.64	107.7	404.06	1.10	1.60	0.316
4-3 (Nat)	353.48	140.9	1665.74	1.25	1.35	0.335
4-4 (Nat)	271.91	145.3	1492.14	1.16	1.26	0.250
4-5 (Nat)	179.01	97.6	1478.11	1.23	1.44	0.245

Table 10 Fitting parameters of grouting-reinforced rock specimens under absorption state

No.	Peak strength /MPa	$E_0$ /GPa	A	B	m	$\alpha (\times 10^{-2})$
4-1 (Abs)	130.77	60	-1.72E+12	4.83	2.29	0.29
4-2 (Abs)	164.19	107.7	-105.75	0.90	1.75	0.20
4-3 (Abs)	332.71	110.5	127.99	0.97	1.14	0.39
4-4 (Abs)	218.69	115.8	73.73	0.75	1.21	0.26
4-5 (Abs)	175.58	123.9	7.16	0.61	1.96	0.19

Table 11 Fitting parameters of grouting-reinforced rock specimens under saturated state

No.	Peak strength /MPa	$E_0$ /GPa	A	B	m	$\alpha (\times 10^{-2})$
4-1 (Sat)	106.99	64.7	-587464.70	2.12	3.38	0.22
4-2 (Sat)	142.66	79.4	-9017.99	1.46	2.64	0.23
4-3 (Sat)	172.84	92.2	339.76	1.00	1.16	0.25
4-4 (Sat)	121.04	74.8	-173906.10	1.95	2.60	0.20
4-5 (Sat)	122.68	77.1	-70400.66	1.84	2.61	0.20

Fig. 12 Relationship between  $B$  and elastic module  $E_0$  at different water bearing states

states are shown. Values of  $p$  and  $q$  in these relationships are both higher at greater water content. And all the correlation coefficients for the absorption and saturated states are greater than 0.8. However, the correlation coefficient for the natural state is low, which suggests that more tests for the natural state should be conducted to confirm the relationship. In addition, the value of  $\alpha$  for different water contents increases with the peak strength, which can be described approximately by a linear relationship  $y = ux + v$ , as shown in Fig. 14.

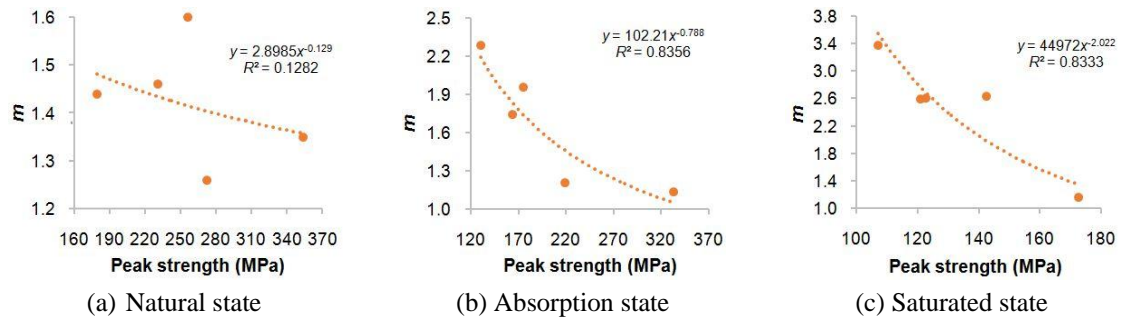


Fig. 13 Relationship between  $m$  and the peak strength at different water bearing states

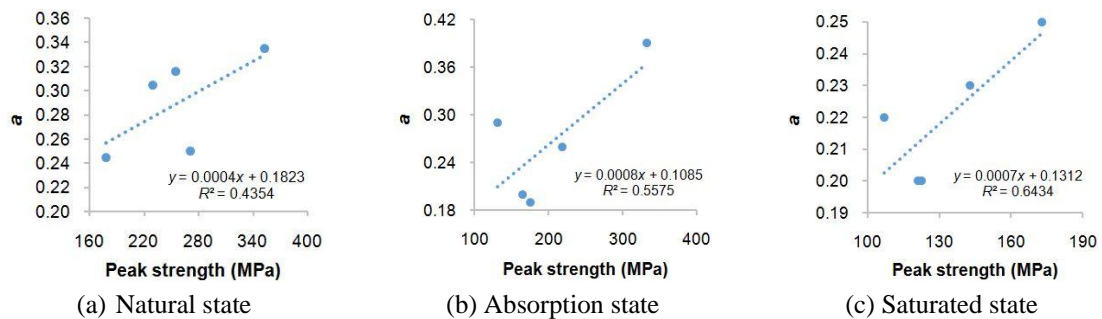


Fig. 14 Relationship between  $\alpha$  and the peak strength at different water bearing states

## 5. Conclusions

Comparison study on the dynamic behaviors of the argillaceous siltstone and its grouting-reinforced body under different water-bearing states was conducted based on experimental tests using SHPB dynamic loading device. The following major conclusions can be drawn based on the results presented in this paper:

- (1) Under dynamic impact, the grouting-reinforced body is generally more fragmented. Most cracks occur in cementation boundaries between the cement mortar and the original rock particles, indicating that the impact resistance is poorer than that of the original rock.
- (2) Water-bearing state has some effects on dynamic behaviors of the argillaceous siltstone and its grouting-reinforced body. Higher water content in both type of samples leads to higher degree of fragmentation, more small broken rock pieces with larger fractal dimensions, and lower dynamic peak strength. However, water content has little effect on the fractal dimensions when the impact velocity is above a certain value.
- (3) When the impact loading rate is increased, the argillaceous siltstone and its grouting-reinforced body will end up with more broken pieces with smaller sizes, i.e., higher degree of fragmentation and larger fractal dimensions. Greater loading rate will also lead to higher peak strength as expected.
- (4) Grouting provides reinforcement to broken rocks to a certain extent. Even it has lower dynamic strength, higher degree of fragmentation and large fractal dimension than the original rock, the grouting-reinforced body has good overall ductility and plastic

deformation capacity, which may provide some desirable properties in engineering applications. The mass ratio of rocks to cement also has significant effects on dynamic properties of grouting-reinforced body. There is an optimal ratio where the peak strength of the grouting reinforced body will reach its maximum.

- (5) The time dependent damage model is only suitable for the description of dynamic behaviors of the original argillaceous siltstone, while the modified overstress damage model is suitable for the description of dynamic behaviors of both the original rock and the grouting-reinforced body. Using the modified overstress damage model, the calculated results are in good agreement with the measured values. The best-fit parameters of the model show some dependence on the water content and the peak strength, which needs to be confirmed by further studies.

The work presented in this paper provides good reference to evaluate the dynamic characteristics of grouting-reinforced rock masses. However, the mechanism of reinforcement was not covered in great detail, which is certainly a topic reserved for future research. Studies on more appropriate and general constitutive model for both the original argillaceous siltstone and its grouting-reinforced body will be of great interests. More tests will also be needed to reinforce the findings discussed in this paper, particularly on samples collected directly from the project site.

## Acknowledgments

The research described in this paper was financially supported by the National Natural Science Foundation of China (NO. 41202195, 41672290, 51404184) and Natural Science Foundation of Fujian province NO. 2016J01189.

## References

- Bailly, P., Delvare, F., Vial, J., Hanus, J.L., Biessy, M. and Picart, D. (2011), "Dynamic behavior of an aggregate material at simultaneous high pressure and strain rate: SHPB triaxial tests", *Int. J. Impact Eng.*, **38**(2-3), 73-84.
- Chen, J., Du, C., Jiang, D., Fan, J. and He, Y. (2016), "The mechanical properties of rock salt under cyclic loading-unloading experiments", *Geomech. Eng., Int. J.*, **10**(3), 325-334.
- Dai, F., Huang, S., Xia, K. and Tan, Z. (2010), "Some fundamental issues in dynamic compression and tension tests of rocks using split Hopkinson pressure bar", *Rock Mech. Rock Eng.*, **43**(6), 657-666.
- Di, Q. and Wang, M. (2010), "Determining areas of leakage in the Da Ye Dam using multi-electrode resistivity", *Bull. Eng. Geol. Environ.*, **69**(1), 105-119.
- Dong, Z.X. and Shan, R.L. (1999), "Study of constitutive properties of rocks under high strain rates", *Eng. Blast.*, **5**(2), 5-9.
- Erguler, Z.A. and Ulusay, R. (2009), "Water-induced variations in mechanical properties of clay-bearing rocks", *Int. J. Rock Mech. Min. Sci.*, **46**(2), 355-370.
- Ghanbarian, B. and Daigle, H. (2015), "Fractal dimension of soil fragment mass-size distribution: A critical analysis", *Geoderma*, **245**(5), 98-103.
- Hsiao, D.H., Phan, V.T.A. and Huang, C.C. (2016), "An experimental investigation on dynamic properties of various grouted sands", *Geomech. Eng., Int. J.*, **10**(1), 77-94.
- Jiang, F. and Vecchio, K.S. (2009), "Hopkinson bar loaded fracture experimental technique: a critical review of dynamic fracture toughness tests", *Appl. Mech. Rev.*, **62**(6), 1469-1474.
- Kikuchi, K., Igari, T., Mito, Y. and Utsuki, S. (1997), "In situ experimental studies on improvement of rock

- masses by grouting treatment”, *Int. J. Rock Mech. Min. Sci.*, **34**(3-4), 138.e1-138.e14.
- Li, X. and Tao, M. (2015), “The influence of initial stress on wave propagation and dynamic elastic coefficients”, *Geomech. Eng., Int. J.*, **8**(3), 377-390.
- Li, W. and Wu, Q. (2013), “Grout improvement effect in jointed rock slope by numerical modelling method”, *Electron. J. Geotech. Eng.*, **18**, 259-268.
- Li, W. and Xu, J. (2009), “Impact characterization of basalt fiber reinforced geopolymeric concrete using a 100 mm-diameter split Hopkinson pressure bar”, *Mater. Sci. Eng. A*, **513**(5), 145-153.
- Liu, Y.R. and Tang, H.M. (1999), *Rock Mechanics*, China University of Geosciences Press, Beijing, China
- Liu, X.H., Zhang, R. and Liu, J.F. (2012), “Dynamic test study of coal rock under different strain rates”, *J. China Coal Soc.*, **37**(9), 1528-1534. [In Chinese]
- Lu, Y.B., Li, Q.M. and Ma, G.W. (2010), “Numerical investigation of the dynamic compressive strength of rocks based on split Hopkinson pressure bar tests”, *International Journal of Rock Mechanics and Mining Sciences*, **47**(5), 829-838.
- Nolen-Hoeksema, R.C. and Gordon, R.B. (1987), “Optical detection of crack patterns in the opening-mode fracture of marble”, *Int. J. Rock Mech. Min. Sci. Geomech. Abstr.*, **24**(2), 135-144.
- Shan, R., Jiang, Y. and Li, B. (2000), “Obtaining dynamic complete stress–strain curves for rock using the Split Hopkinson Pressure Bar technique”, *Int. J. Rock Mech. Min. Sci.*, **37**(6), 983-992.
- Shan, R.L., Xue, Y.S. and Zhang, Q. (2003), “Time dependent damage model of rock under dynamic loading”, *Chinese J. Rock Mech. Eng.*, **22**(11), 1771-1776. [In Chinese]
- Utsuki, S. (2013), “In-situ experimental studies on improvement of deformability of rock masses by grout treatment”, *Int. J. JCRM*, **9**(1), 7-8.
- Wang, Q.Z., Zhang, S. and Xie, H.P. (2010), “Rock dynamic fracture toughness tested with holed-cracked flattened Brazilian discs diametrically impacted by SHPB and its size effect”, *Experim. Mech.*, **50**(7), 877-885.
- Wong, R.H. and Chau, K.T. (1998), “Crack coalescence in a rock-like material containing two cracks”, *Int. J. Rock Mech. Min. Sci.*, **35**(2), 147-164.
- Xie, H.P. (1993), *Fractals in Rock Mechanics*, CRC Press, Beijing, China.
- Xu, H.F., Geng, H.S., Li, C.F., Chen, W. and Wang, C. (2013), “Estimating strength of grouting reinforced bodies in broken rock mass”, *Chinese J. Geotech. Eng.*, **35**(11), 2018-2022. [In Chinese]
- Yang, X. and Li, Y. (2008), “Construction and quality analysis of curtain grouting in foundation of dam for Yangtze Three Gorges Project”, *J. Child Family Studies*, **18**(6), 978-981.
- Zhang, M., Wu, H.J., Li, Q.M. and Huang, F.L. (2009), “Further investigation on the dynamic compressive strength enhancement of concrete-like materials based on split Hopkinson pressure bar tests. Part I: Experiments”, *Int. J. Impact Eng.*, **36**(12), 1327-1334.
- Zhao, G., Xie, L. and Meng, X. (2014), “A damage-based constitutive model for rock under impacting load”, *Int. J. Min. Sci. Technol.*, **24**(4), 505-511.
- Zhou, Z., Li, X., Liu, A. and Zou, Y. (2011), “Stress uniformity of split Hopkinson pressure bar under half-sine wave loads”, *Int. J. Rock Mech. Min. Sci.*, **48**(4), 697-701.
- Zolfaghari, A., Bidar, A.S., Javan, M.M., Haftani, M. and Mehinrad, A. (2015), “Evaluation of rock mass improvement due to cement grouting by Q-system at Bakhtiary dam site”, *Int. J. Rock Mech. Min. Sci.*, **74**(2), 38-44.